

Article

Automated Sensing of Wave Inundation across a Rocky Shore Platform Using a Low-Cost Camera System

Hannah E. Power ^{1,*} , Michael A. Kinsela ², Caio E. Stringari ¹, Murray J. Kendall ¹, Bradley D. Morris ² and David J. Hanslow ² 

¹ School of Environmental and Life Sciences, University of Newcastle, Callaghan, NSW 2308, Australia; caio.eadistringari@uon.edu.au (C.E.S.); murray.kendall@uon.edu.au (M.J.K.)

² Office of Environment and Heritage, NSW Government, Sydney, NSW 2000, Australia; michael.kinsela@environment.nsw.gov.au (M.A.K.); bradley.morris@environment.nsw.gov.au (B.D.M.); david.hanslow@environment.nsw.gov.au (D.J.H.)

* Correspondence: hannah.power@newcastle.edu.au; Tel.: +61-(0)2-4921-5606

Received: 7 November 2017; Accepted: 12 December 2017; Published: 23 December 2017

Abstract: Rocky coastlines are frequently used for recreation, however, they are often highly exposed and hazardous environments resulting in high risk to visitors. Traditional approaches to managing human safety in coastal settings (such as the surf lifesaving clubs that have proven effective on beaches) are not necessarily transferable to rock platforms due to their often remote and fragmented distribution and the different recreational uses. As such, a different approach is required. To address this, we present a low-cost camera system to assess the wave hazard on a high-visitation rocky shore platform: the Figure Eight Pools Rock Platform, New South Wales, Australia. The camera system is shown to be highly effective and allows identification of both the distance and frequency of wave inundation on the platform using a novel pixel analysis technique. Nearshore wave height is shown to be the primary factor driving inundation frequencies along the cross-platform transect investigated with some influence from wave period. The remotely sensed camera data are used to develop a preliminary overwash hazard rating system, and analysis of the first month of data collected suggests that the platform is highly hazardous to visitors. Future work will expand this hazard rating system, developing a predictive tool that estimates the overwash hazard level based on forecast wave and tide conditions to improve visitor safety at the site.

Keywords: coastal hazards; rocky shore platforms; camera monitoring; wave overwash

1. Introduction

Temperate rocky coastlines are typically exposed environments that are subject to high wave energy. These coastlines are often characterized by cliffs with sub-horizontal platforms at the base of the cliff (hereafter rock platforms) that often sit at approximately mean sea level but exist at a range of elevations [1,2]. As waves approach rock platforms, some wave energy may be dissipated prior to waves reaching the platform, depending on the grade and substrate of the offshore seabed. However, the majority of wave energy is often dissipated by waves breaking at the edge of the platform and as waves progress across the platform [3].

Rock platforms attract a range of recreational uses, such as rock fishing, inter-tidal foraging and walking, but they are often hazardous environments as a result of high exposure to waves. For example, infrequent or intermittent wave overtopping of platforms may catch recreational visitors by surprise, sweeping them across rugged platform surfaces or into the sea, and resulting in serious injuries or death. Between 1992 and 2000, there was an average of eight deaths per year on rock platforms in New South

Wales (NSW), Australia [4] and, between 2004 and 2014, 19% of all coastal related deaths in Australia occurred on rock platforms [5,6]. Non-fatal injuries, while less documented, can still represent a significant burden to emergency services, as rock platforms in remote locations may be accessible only by foot or air.

Traditional approaches to managing human safety in coastal settings, such as paid lifeguards and volunteer surf lifesaving movements, were developed for recreational activities in beach settings. However, such approaches are not necessarily transferrable to rock platforms, due to the often remote and fragmented distribution of rock platforms, and the different recreational uses. Given this, an alternate approach to managing safety on rock platforms is required, particularly in locations where aspects of the natural amenity attract high visitation by a broad range of visitor types.

An alternative approach to managing visitor safety is to develop tools that predict and communicate the hazard level on individual platforms based on the relationship between platform morphology and forecast wave and tide conditions. This is analogous to managing forest fire hazard with the Forest Fire Danger Index (FFDI), which uses forecast fire weather parameters and the vegetation fuel state to determine and communicate the forest fire risk level [7]. Similarly, developing a wave hazard risk rating for rock platforms requires sufficient data and understanding of the influence of the local wave and tide conditions on wave overtopping at the platform of interest. Obtaining data on the time varying wave hazards on a rock platform may be challenging due to the exposed setting and potential difficulty in deploying instruments that record data in situ. For example, wave sensors may be temporarily deployed with relative ease in beach settings using movable frames or metal stakes inserted into the sandy substrate; however, deploying such instruments on a rock platform may require a more permanent and invasive approach, such as drilling into the platform to create secure fixtures, and the instruments may be vulnerable to human disturbance during low tides or calm conditions. Remote sensing provides an attractive alternate means of measuring wave processes and hazards on rock platforms.

Remote sensing techniques, including the use of video cameras, have been widely used in coastal studies with data collection and analysis techniques advancing rapidly in recent years [8,9]. One of the main advantages of remote sensing techniques is that they allow for the collection of large volumes of data across a wide spatial and temporal domain with relative ease and from an accessible position. They also allow for data collection during extreme conditions and in environments where collecting in situ data would be highly challenging, such as in large storm events (e.g., [10]) and on coral reefs (e.g., [11]). Video remote sensing techniques are one of the more common remote sensing techniques used in the coastal zone and have been used to investigate various processes including: bar morphodynamics [12], wave run-up [13], swash zone flow velocities [14], and the evolution of surf zone rips [15,16]. However, the majority of coastal research that uses video remote sensing techniques relies on expensive “off-the-shelf” camera systems that typically require complex installations with permanent infrastructure to manage power supply, camera operation, and data storage and telemetry.

Here, we describe the development and application of a low-cost coastal camera monitoring system to investigate wave overwash hazards at a remote but high-visitation exposed rocky shore platform near Sydney, Australia. The popularization of the unique naturally-formed rock pools at the site has led to a rapid increase in visitation and a need to manage visitor safety. A number of visitors have sustained minor to serious injuries including lacerations, broken bones, and head injuries, when they have been surprised by waves overtopping and washing across the platform.

To investigate the relationship between ocean wave and water level conditions, and wave overwash at the site, we develop and apply a simple but effective camera monitoring system to measure wave overwash on the platform, concurrent with nearshore wave observations using a wave buoy. We also carry out hydrodynamic measurements across the platform to evaluate the efficacy of the camera system and the image analysis techniques for identifying and measuring overwash on rock platforms. We present a five-month dataset of processed imagery that provides an hourly overwash hazard rating based on the coverage and frequency of overwash on the platform. We analyze the processed dataset to investigate the sensitivity of wave overwash to ocean wave and water level conditions, and to identify the hydrodynamic conditions that drive variability in wave overwash

hazard. The research findings will be applied in an overwash hazard rating system to improve visitor safety at the site.

This paper is organized as follows. Section 2 describes the study site, local environmental conditions, and the nearshore hydrodynamic climate. The camera system, image analysis, and hydrodynamic data collection are described in Section 3. Section 4 details the efficacy of the camera system and a comparison between the remotely sensed camera data and the in situ hydrodynamics measurements. The frequency of platform inundation through time and the relation to the hydrodynamic conditions is explored in Section 4.3. Results are discussed in Section 5 and final conclusions follow in Section 6.

2. Field Setting

The camera systems and hydrodynamic instruments were deployed to investigate the wave overwash hazard at Figure Eight Pools Rock Platform located in the Royal National Park 1 hour south of Sydney, Australia (Figure 1). The site features a variety of unique natural rock pools, including the namesake Figure Eight Pool, which have been weathered into the sandstone platform over thousands of years. Popularization of the rock pools on social media in recent years, particularly through photo sharing platforms, has attracted a high volume of local and international visitors, who primarily visit to bathe in the pools and have their photo taken (e.g., Instagram photos and videos: <https://www.instagram.com/explore/tags/figure8pools/?hl=en,#figure8pools>). The hazardous setting, unique platform morphology, and high visitation, all present challenges to managing visitor safety at the site.

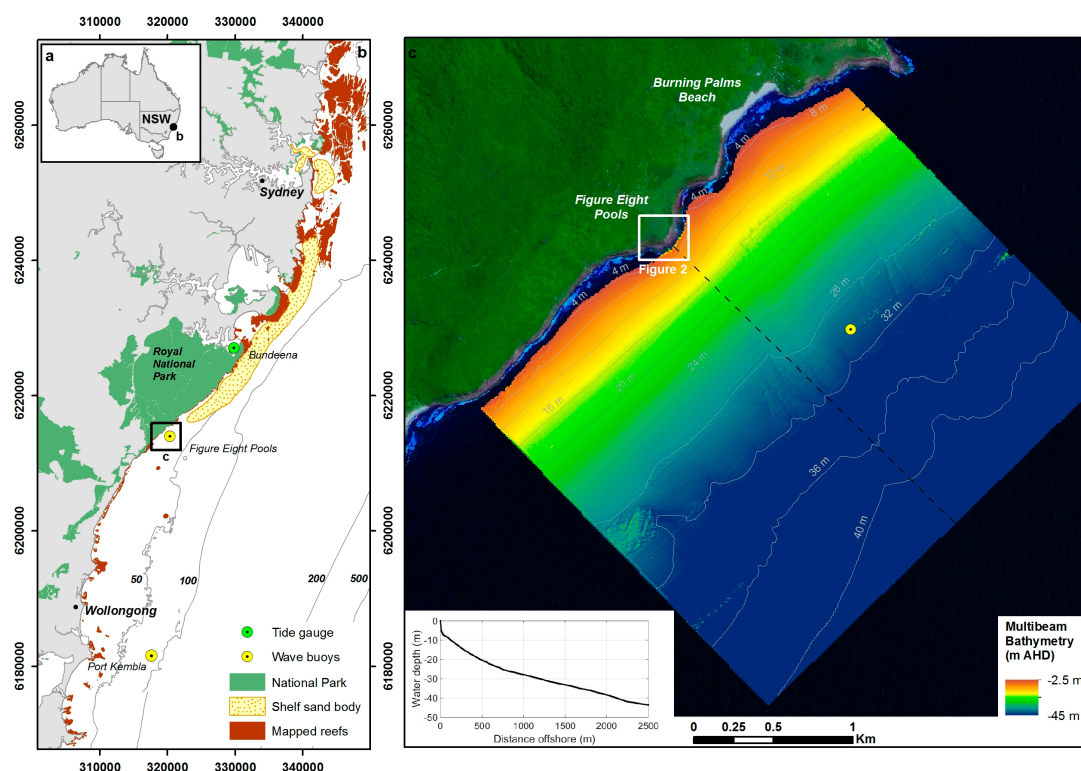


Figure 1. (a,b) The Figure Eight Pools Rock Platform is located in the Royal National Park, approximately 50 km south of Sydney, NSW, Australia. (b) The coastline trends northeast-southwest and is fully exposed to waves arriving from the northeast to south directions, as measured by the Port Kembla permanent wave buoy. (c) A directional wave buoy was deployed temporarily in 30 m water depth adjacent to the Figure Eight Pools Rock Platform to measure local wave conditions, and the inner-shelf seabed was surveyed using a multibeam echosounder. Inset shows a shore-normal bathymetric profile along the dashed line. Adapted from [17].

Elevation data from LiDAR and RTK-GNSS surveys [17] show that the rock platform has a relatively flat, wide, and predominantly supratidal sandstone surface, with a curved northeast-southwest orientation that fringes coastal cliffs of 40 m elevation (Figure 2). The platform extends about 50 m on average from the base of the cliffs to the shore, where it drops abruptly into the sea. The topography of the platform is complex, with the northeast section higher than the southwest section, and the seaward edge often higher than the mid-platform elevation due to the presence of a rampart (Figure 2). Platform elevation is mostly above the highest astronomical tide (HAT) in this microtidal setting (2 m maximum tidal range), which is around 1 m above Australian Height Datum (AHD) or approximately mean sea level. Nonetheless, the platform is exposed to the full range of wave directions (northeast to south) within a moderate-high energy wave climate, with mean $H_s = 1.6$ m and $T_s = 8$ s at the Port Kembla wave buoy (Figure 1b). The orientation and irregular elevation of the seaward edge suggest that the platform is particularly exposed to overwash from waves that predominantly arrive from south to southeast directions in this region (Figures 1 and 2).

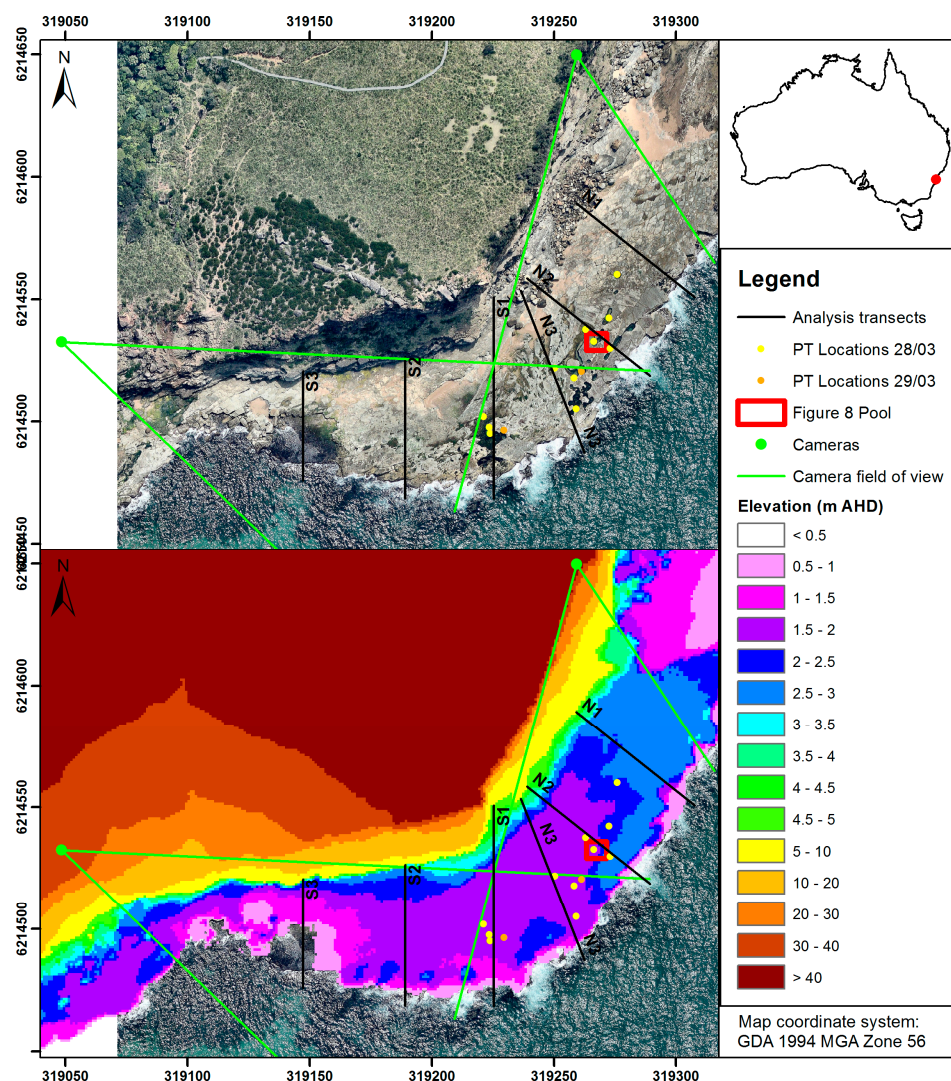


Figure 2. Site map of the Figure Eight Pools Rock Platform showing the camera locations and fields of view, locations of pressure transducers, the timestack transect lines, and the location of the Figure Eight Pool. The upper panel shows an aerial image (Source: NearMap) of the site captured on 10 October 2016 and the lower panel shows LiDAR elevation data relative to the Australian Height Datum (AHD). The inset in the upper right corner shows the location of the site within Australia.

2.1. Rock Platform Geomorphology and Access

The seaward edge of the platform is near-vertical, and is well defined in the vicinity of the mean sea-level shoreline, consistent with ‘type-B’ platform morphology [1,18]. The water depth adjacent to the seaward edge is approximately 5 m, and the nearshore seabed slopes steeply to around 7–8 m water depth. The inner-continental shelf fronting the platform has an average slope of 1:50 to 50 m water depth (Figure 1c). The seabed substrate is sandy, with sedimentological properties consistent with an inner-shelf sand body (Figure 1b) that was mapped and sampled to the north along this coastal sector [19]. The escarpment, cliffs, and rock platform form part of the East Australian marine abrasion surface formed of Mesozoic-Paleozoic sedimentary rocks cut and planed by cyclic marine erosion that extends 300 km along the coast north and south of Sydney, and up to 23 km offshore beneath the shelf sediments [20].

Access to the platform is via a steep and rugged escarpment trail to Burning Palms Beach (Figure 1c), followed by a challenging traverse around the base of coastal cliffs and a boulder beach. The total journey takes more than one hour each way for a fit adult. There is no road access, utilities, or visitor facilities at the site. A small heritage community at the northern end of Burning Palms beach is fully self-sufficient, relying on solar electricity and rainwater. The remote location and difficult access to the site means that emergency response to injured visitors is costly and resource-intensive. For example, at least 20 severe incidents in the 2016 calendar year resulted in rescues by helicopter or ground teams.

The remote location and difficult access also present challenges to investigating wave hazards on the rock platform, and necessitated that the camera systems be fully self-sufficient and capable of withstanding the harsh environment with minimal maintenance. While a helicopter was used to transport the solar-battery power system components to the camera sites for installation (see Section 3.1), all other site visits by the project team were made by foot.

2.2. Nearshore Hydrodynamic Climate

To obtain information on the nearshore hydrodynamics that drive wave overwash on the Figure Eight Pools Rock Platform, a temporary wave buoy (Datawell DWR-G4) was deployed on 6 December 2016 in 30 m of water adjacent to the platform (Figure 1c). The wave buoy is serviced and de-fouled every 5–6 weeks, most recently on 30 October 2017, and provides a continuous record of nearshore wave conditions for the duration of the camera datasets. A permanent deep-water wave buoy is maintained in 80 m water depth off Port Kembla, approximately 40 km south of the temporary wave buoy (Figure 1b), providing long-term regional wave climate information.

Ocean tide data were obtained from the Bundeena tide gauge operated by Manly Hydraulics Laboratory for the duration of the camera deployment. Data have a sampling frequency of 15 min. This gauge is located ~16 km to the north of the Figure Eight Pools Rock Platform (Figure 1b).

Data from the wave buoy located in 30 m depth off the platform reveal a moderate energy wave climate with a dominant south-southeasterly direction (Figure 3). The mean significant wave height (H_s) was 1.33 m the modal H_s was 1.0–1.1 m. A wave height of $H_s = 1.19$ m was exceeded 50% of the time. Mean and modal spectral mean wave period (based on the first positive moment of the energy spectrum, T_{m01}) were 6.7 s and 5.75–6 s respectively. Mean spectral peak wave period (T_p) was 10.0 s and T_p exceeded 14 s for 7.4% of the time. Mean peak wave direction (D_p) was 135° and modal peak wave direction was 150–160° (Figure 3).

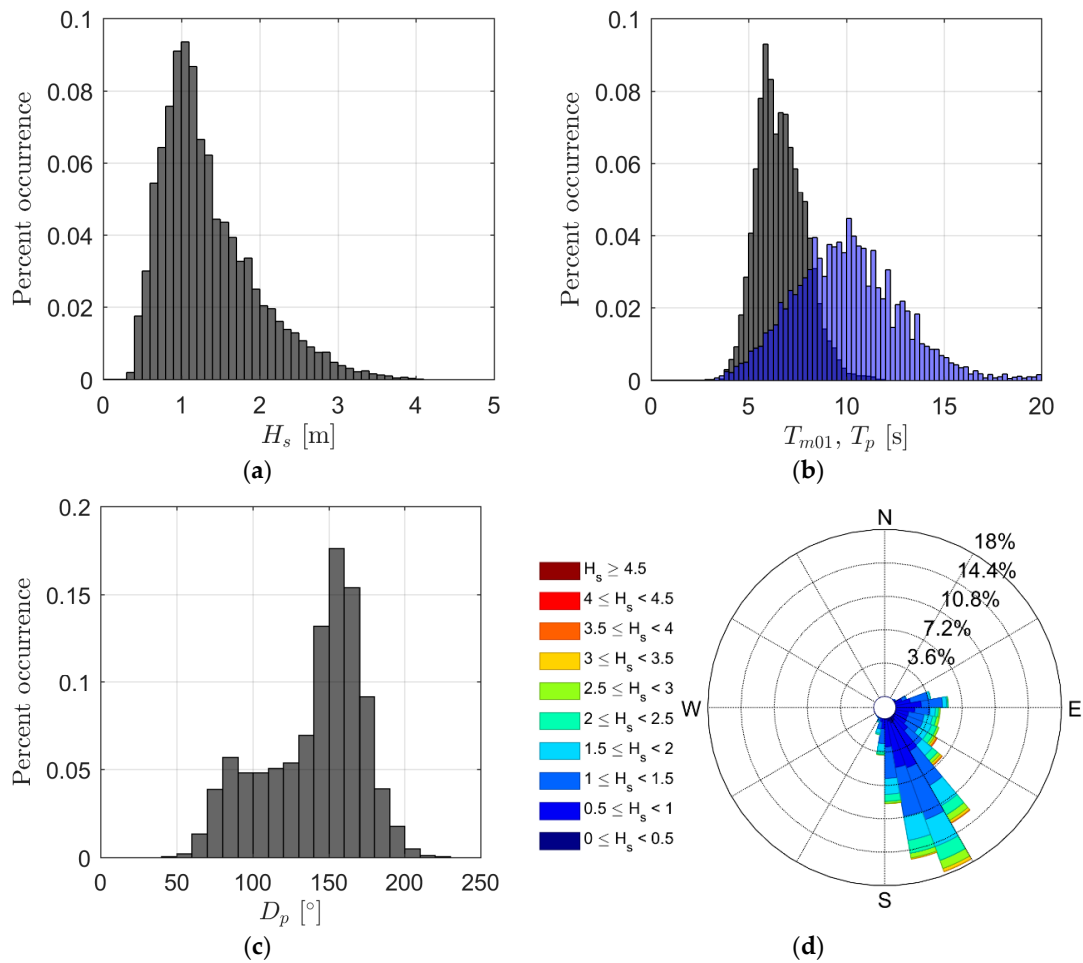


Figure 3. Local wave conditions at the site: histograms of percent occurrence for (a) significant wave height (H_s), (b) spectral mean wave period based on the first positive moment of the energy spectrum (T_{m01} ; grey bars) and spectral peak wave period (T_p ; blue bars), and (c) peak wave direction (D_p); and (d) a wave rose of H_s . See Figure 1c for wave buoy location relative to the rock platform. Data are for the period 6 December 2016 to 30 October 2017.

3. Methods

3.1. Camera System and Installation

Given the challenges of collecting in situ field data describing wave overwash hazards on rocky shore platforms, camera remote sensing is an ideal alternative for data collection. To investigate overwash hazards at Figure Eight Pools Rock Platform, we developed a low-cost remote sensing system comprising two camera systems, to obtain full coverage of the area of interest (Figure 2). Each system consists of a 3.2 megapixel FLIR (formerly PointGrey) Flea3 color image camera fitted with a Fujinon 6 mm lens (Figure 4a,b respectively). Camera image capture is controlled by a Raspberry Pi computer (Figure 4c,d) using custom C++ and Python code to control capture frequencies and data storage. We captured images at 1 Hz for the first 20 min of each daylight hour, to balance data storage with image analysis needs; however, these values are programmable in the software code and could be adapted to suit other purposes. Captured images were stored on site using a 128 GB USB flash drive connected to each Raspberry Pi computer, which could store approximately 325 20-min capture cycles (at 1 Hz), amounting to between 25 and 36 days of image capture based on 10–14 daylight hours. The USB sticks were retrieved and replaced every 2–4 weeks to collect the image data for subsequent analysis. The itemized cost of the camera system (as of the time of writing) is shown in Table 1.

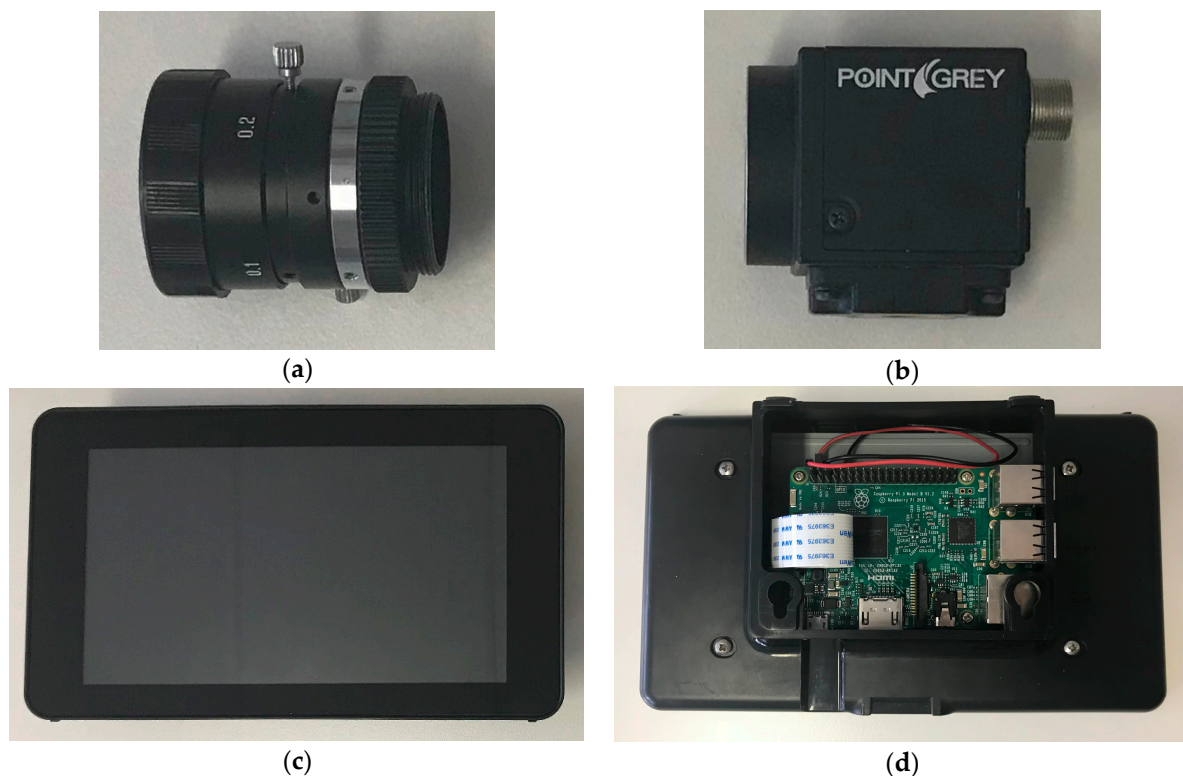


Figure 4. Components of the camera system: (a) camera lens, (b) camera, (c) Raspberry Pi computer touch screen, and (d) Raspberry Pi computer and case.

Table 1. Approximate cost of the components of the camera system excluding any taxes. Site installation costs are not included. Prices shown are costs obtained as at the time of publication. Items purchased in AU\$ were converted to US\$ at the rate of AU\$1:US\$0.78.

Component	Cost (US\$)
Camera (FLIR Flea3)	\$465
Lens (Fujinon 6 mm)	\$190
Computer (Raspberry Pi, touch screen, case)	\$144
Storage (128 GB USB flash drive)	\$59
Camera housing	\$185
Mobile telephone modem ¹	\$63
Solar panel and frame (200 W, 24 V)	\$424
Solar regulator (15 A)	\$127
Cabling for solar panels to batteries	\$152
Gel batteries (12 V, 138 Ah, ×2)	\$523
Power converters (12 V to 5 V)	\$34
Battery housing (ventilated steel locker)	\$386
Assembly and testing of solar power system	\$315
Total	\$3067

¹ Does not include data costs.

The remoteness of the site poses challenges to the installation and maintenance of camera monitoring systems, so we designed the low-cost camera systems to mitigate some of the logistical difficulties of remote deployment. One challenge is that the site could only be visited by the project team relatively infrequently (approximately every 2–4 weeks), thus limiting the frequency of raw camera data collection and camera maintenance. To mitigate risks to the datasets posed by infrequent maintenance, we included a data telemetry capability in the design to allow the project team to remotely

monitor site conditions and the status of the camera systems. Sample images, capture metadata, and system information (such as remaining storage capacity on the USB drives) are telemetered via email using a mobile telephone network modem at the end of each data capture cycle.

Another challenge was the lack of mains power at the camera sites. As such, each camera system is powered by a 200 W 24 V solar panel (Figure 5a) connected to a 15 A solar regulator and two 12 V 138 Ah gel batteries (Figure 5b), with 12 V to 5 V converters to supply power to the camera and computer at the required voltages. The system was designed to contain sufficient backup power to cover periods of poor weather and low incident sunlight even during the winter months, with sufficient power from fully charged batteries to cover eight days with no battery recharge from the solar panels. The camera sites are situated near the edge of the coastal cliff and are exposed to high winds and salt spray. To protect the camera and power system components, all electronics are stored in a standard, ventilated steel locker, with the cameras mounted in standard security camera housings (see Figure 5c,d). The computer components were further sheltered from moisture and salt spray by a plastic box inside the steel locker (Figure 5b). The electronics lockers and camera housings were painted to further minimize the low visual impact of the camera systems on the natural aesthetics of the site.



Figure 5. Camera setup on site showing (a) the solar panel; (b) the gel batteries, solar regulator, and power converters; and the cameras mounted in the security camera housings and the battery housing box for (c) the north camera and (d) the south camera.

3.2. Image Analysis

All imagery captured by each camera was rectified using the method of Holland et al. (1997) with known ground control points obtained with a Trimble real-time kinematic GNSS system during the camera installation process. Rectified images had pixel resolutions that varied from 0.5 m^2 in the near field to 10 m^2 in the far field of view with pixel resolutions on transect N2 (see Figure 2) ranging from $0.25 \times 0.25 \text{ m}$ to $0.3 \times 0.5 \text{ m}$. For each image capture cycle (i.e., 20 min of imagery captured at 1 Hz), timex (average) and variance images were created from these series of rectified images. To assess the degree of wave overwash on the platform, timestacks were created from each series of rectified images along three transect lines for each camera using the method of [21] (see Figure 2 for location of transect lines).

To automatically obtain the degree of wave overwashing on the rock platform along each transect line, pixel values in the timestack were used to identify the percentage of time the platform was inundated at each cross-platform location, thus resulting in a cross-platform inundation frequency (XPIF) profile. To achieve this, each pixel in each timestack was first converted from RGB color values to the CIECAM02 color space (the Color Appearance Model (CAM) published by the International Commission on Illumination (CIE) Technical Committee, [22]) and then analyzed using two metrics: (1) a pixel lightness metric and (2) a pixel color temperature metric. The lightness metric was the primary metric used to assess the degree of wave overwashing and was defined as the Euclidian distance between a black pixel and the color value of a given pixel in the CIECAM02 color space. This results in a measure known as color similarity (ΔE) that varies from 0 to 100 [23]. White or nearly white pixels, such as those that are representative of breaking waves, have values close to 100 in this lightness metric. At each cross-platform location, the frequency of inundation over the duration of the timestack was defined as the percentage of time during which ΔE was at least two times greater than a baseline ΔE value. The baseline ΔE value was calculated at each cross-platform location within a given timestack using a polynomial regression fitted to the minimum values in the ΔE time series. This allowed for light variations across the platform (for example, due to late afternoon shadows on the platform) and through time (for example, due to changes in cloud cover). In cases where the averaged ΔE for the full time series was $\Delta E > 80$ or $\Delta E < 30$, the lightness baseline assumed these values, respectively. This was done to prevent incorrect classification of instances where the platform had either no inundation or complete and constant inundation.

In some instances, however, high values of ΔE were observed to occur due to factors other than wave inundation, such as sunlight reflecting from the dry rock platform or from still water in the rock pools. To avoid these instances as being incorrectly classed as high levels of inundation, the second metric, pixel color temperature, was used. Pixel color temperatures were obtained by translating RGB values into temperatures based on the Planckian Locus transformation [24] and these values allow for differentiation between bright but cool pixels (such as those that correspond to wave breaking) and bright but warm pixels (such as those that correspond to brightly lit rocks). The frequency of inundation was calculated using the pixel color temperature matrix in the same manner as for the pixel lightness metric, and this was used to further refine the frequency of inundation as calculated by the pixel lightness metric. Firstly, if a location on the platform was classified as inundated by both the lightness and color temperature metrics, inundation values from the pixel lightness metric were retained. Secondly, if a location on the platform was classified as inundated by only the lightness metric (i.e., the color temperature metric indicated no inundation was occurring), the color temperature metric was used to classify that location as not inundated. Lastly, if a location on the platform was classified as inundated only by the color temperature metric (i.e., the lightness metric indicated no inundation was occurring), the lightness metric was used to classify that location as not inundated.

The combination of these two metrics corrected the majority of instances where the platform was incorrectly automatically classified as being inundated due to factors other than breaking waves; however, there were still instances where the two metrics incorrectly classified the platform as inundated, these primarily occurred due to sunlight reflecting from still water in the rock pools.

To address this, all timestacks and their derived XPIFs, were analyzed to identify instances where there was a gap in inundation levels across the platform. All instances were manually checked and incorrect classifications were removed. Across the full dataset for transect N2, there were 295 instances of this issue that were automatically identified but manually corrected.

3.3. Pressure Transducer Data Collection

To verify the camera data, two pressure transducer deployments were conducted. On 28 March 2017, 6 INW PT2X sensors and 5 RBR*solo* D1 wave sensors all self-logging with a sampling frequency of 8 Hz were deployed between 11:25 and 16:30. To preserve the natural aesthetics of the site, all sensors were temporarily deployed by attaching them to lead weights and placing them in the bottom of the pools (see Figure 2 for sensor locations). These 11 sensors were retrieved on 29 March between 15:25 and 16:25. Two RBR*solo* D1 wave sensors were deployed at 17:00 on 29 March 2017 with a sampling frequency of 8 Hz with the goal to collect data during a forecast swell event (see Figure 2 for sensor locations). These sensors were deployed in the same manner as the previous deployment and were retrieved on 7 April 2017 at 15:00. These PT data were used to compare water surface elevation records with pixel intensity time-series extracted from the camera data at the location of the PT as a means of ground-truthing the camera data (see Section 4.2).

4. Results

4.1. Efficacy of Camera System and Camera Outputs

The north and south cameras were installed on 21 March 2017, after completing installation of the solar-battery power systems the week prior, and both cameras remain operational as of 12 October 2017. A total of 5 instances of camera outages occurred across both cameras since installation with 96% and 88% data coverage over the observation period for the north and south cameras respectively. In each instance, the most likely causes of outages were either low battery power due to prolonged low sunlight, or power leakage through the solar regulator or 12 V to 5 V converters, resulting in insufficient power supply to the Raspberry Pi computer. In these cases, the Raspberry Pi computer shut down and failed to reboot automatically, requiring manual reboot during a service visit. During daytime maintenance visits the power system batteries were almost always fully charged.

The cameras captured a wide range of conditions on and adjacent to the rock platform, from very calm and benign, to storm conditions with nearshore significant wave heights up to $H_s = 4.73$ m. Example oblique images showing the range of conditions captured are shown in Figure 6. Rectified timex and variance images, derived from the full 1200 images captured in each cycle, are shown in Figure 7. The timex images clearly identify regions of wave breaking (light/white pixels) and are useful for quickly identifying instances of high wave overwash on the platform. The variance images highlight regions of pixels with high variance through time, such as regions of wave breaking, but also changes in light intensity, such as the impact of varying cloud cover on the rock platform (see Figure 7a, right panel, where close to the cliff at approximately 319,245 m E, 6,214,535 m N, high variance is observed but no overwash is observed in the timex).

An example 20-min timestack, obtained from transect N2 during a period of intermittent overwashing, is shown in Figure 8a. Near continuous wave breaking seaward of the platform edge can be seen by the white pixels at $x < 0$ m for the full duration of the timestack. Intermittent wave overwashing can be seen throughout the length of the timestack (white wave paths running in near vertical lines down the timestack from the platform edge at $x = 0$ m). The majority of overwash events are relatively small, only inundating the seaward edge of the platform to $x \sim 7$ m; however, nine events extend significantly further on to the platform, to $x \sim 24$ m. This timestack describes intermittent overwash conditions of variable magnitude.

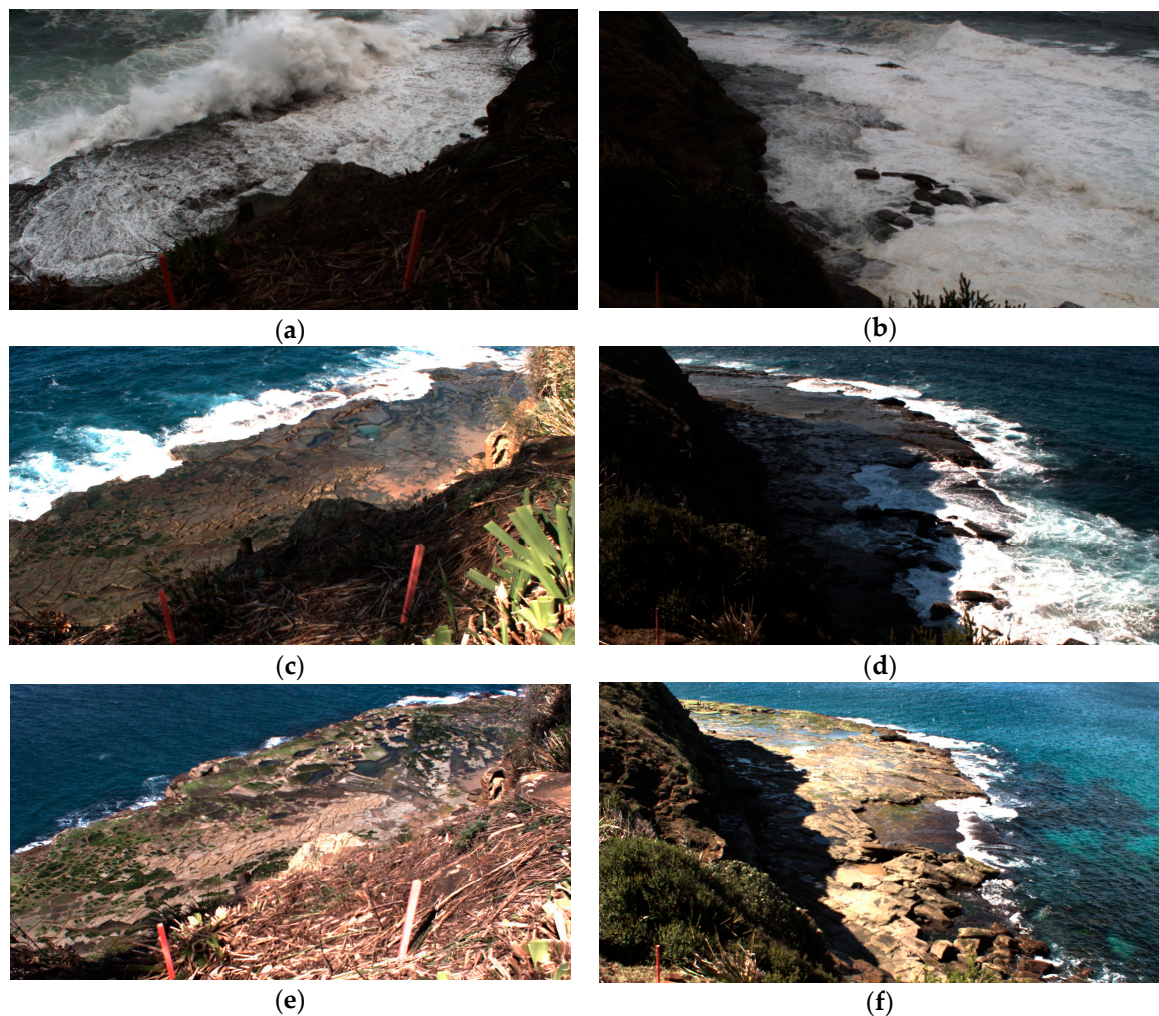


Figure 6. Examples of frames collected by the camera system under different conditions: high energy conditions ($H_s = 3.12$ m, $T_{m01} = 9.2$ s, $D_p = 160^\circ$) on 27 April 2017 at 17:00 at (a) the north camera and (b) the south camera; moderate energy conditions ($H_s = 1.41$ m, $T_{m01} = 6.62$ s, $D_p = 150^\circ$) on 11 May 2017 at 10:00 at (c) the north camera and (d) the south camera; and low energy conditions ($H_s = 0.47$ m, $T_{m01} = 4.8$ s, $D_p = 100^\circ$) on 10 April 2017 at 11:00 at (e) the north camera and (f) the south camera.

Using the method described in Section 3.2, pixel values in the timestack were converted to lightness values and color temperature values, which were used to calculate the frequency of inundation. The cross-platform values of these two metrics for the example timestack are shown in Figure 8b with the final combined metric shown in Figure 8c. The pixel analysis metrics yield high frequencies of inundation (close to 100%) seaward of the platform edge which corresponds well to the observations of the timestack that suggest near continuous wave breaking seaward of the platform edge (Figure 8a,b). Landward of the platform edge, the frequency of inundation drops to below 40% and continues to decrease as distance onto the platform increases, as per the observations of the timestack, indicating decreasing frequency of intermittent overwashing. The use of color temperature to disregard erroneous overwash is demonstrated at $27 < x < 34$ m and $37 < x < 47$ m (shown by the grey shaded areas in Figure 8b and the final inundation frequencies in Figure 8c). Small peaks in XPIF between the edge of the platform and the landward limit of inundation correlate with pools and slight changes in elevation across the platform (Figure 8c). The erroneous spike at $x \sim 35$ m, which is due to high pixel lightness and color temperature potentially caused by standing water on the

platform (grey bars in Figure 8c), was removed by automated quality control methods to obtain the final cross-platform inundation frequency profile (black bars in Figure 8c).

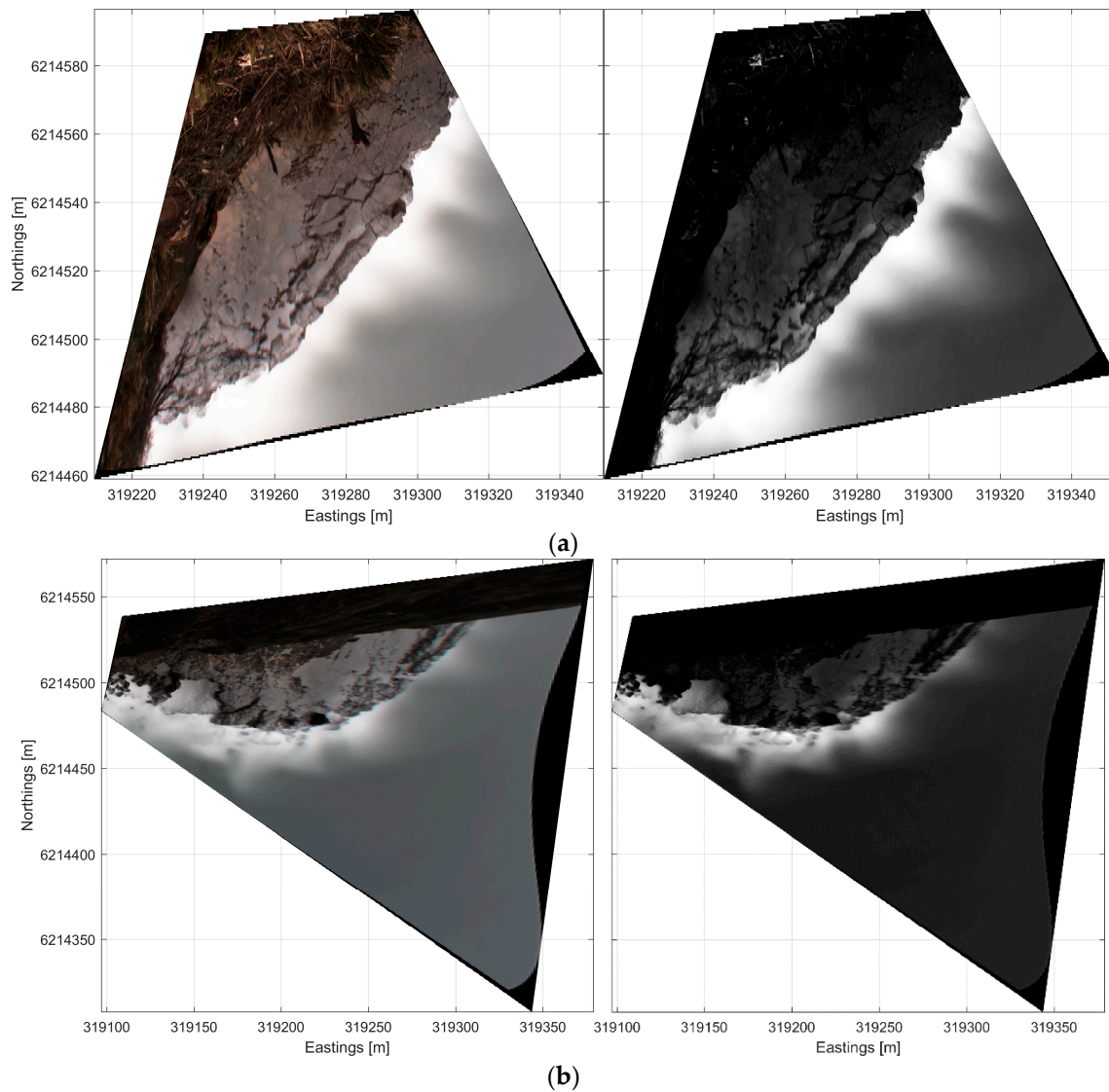


Figure 7. Example timex (left panels) and variance (right panels) images created from the camera data for (a) the north camera and (b) the south camera 12:00 on 23/03/2017. Eastings and northings correspond to the coordinate system GDA94 MGA Zone 56.

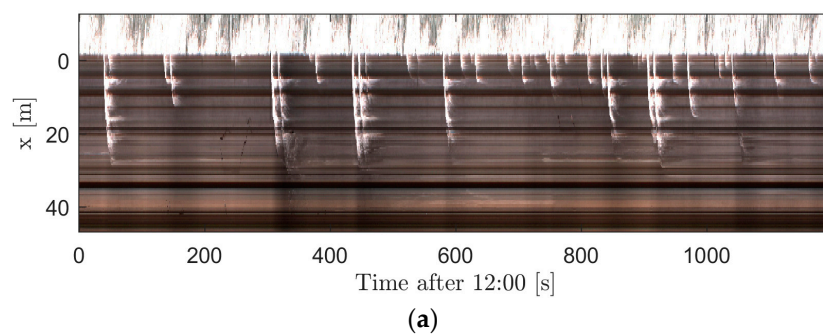


Figure 8. Cont.

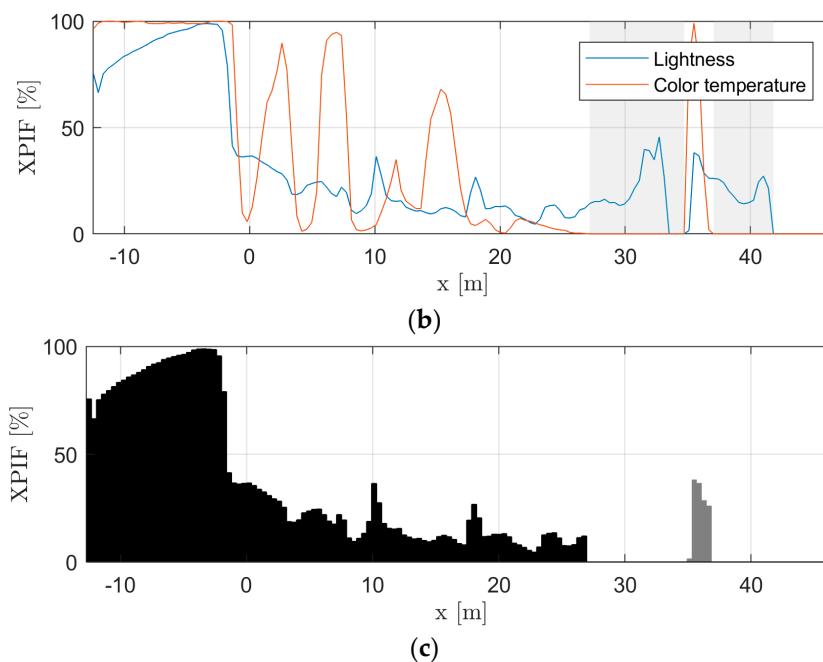


Figure 8. (a) Example timestack from transect N2 taken at 12:00 on 23/03/2017 showing intermittent overwashing on the rock platform at this location, (b) cross-platform inundation frequency (XPIF) as defined by the pixel lightness metric and the pixel color temperature metric, and (c) resultant combined XPIF profile (grey and black bars) with the grey bars removed via automatic quality control processes to obtain the final XPIF profile (black bars). See Figure 2 for transect location.

4.2. Comparison of Remotely Sensed and In Situ Observations

To assess the use of the pixel lightness values from the camera data as a proxy for wave overtopping on the rock platform, pixel time series were extracted from the rectified camera imagery at the location of the pressure transducers, and the pixel lightness time series were compared to the water surface elevation time series derived from the PT data. An example of these two paired time series is shown in Figure 9. It is clear from comparison between the measured (transducer) and the remotely sensed (camera) data, that the peaks in the measured water surface elevation time series are accompanied by simultaneous peaks in the pixel lightness time series. Despite a strong correspondence between the peaks in the pixel lightness and those in the water surface elevation time series, the peaks in the pixel lightness time series are typically of longer duration than the corresponding peaks in the water surface elevation time series. This has the potential to result in overestimation of the duration of inundation; however, for the purpose of this project, this measure was deemed to be fit for purpose. This is discussed further in Section 5. Equivalent assessments were performed for PT and pixel paired time series for other PT locations and other times and similar observations were made. These data indicate that pixel lightness values are a suitable proxy of the occurrence of wave overwashing at positions across the platform, and thus can be used to classify the overwash hazard level measured as the distance and frequency of platform overwashing.

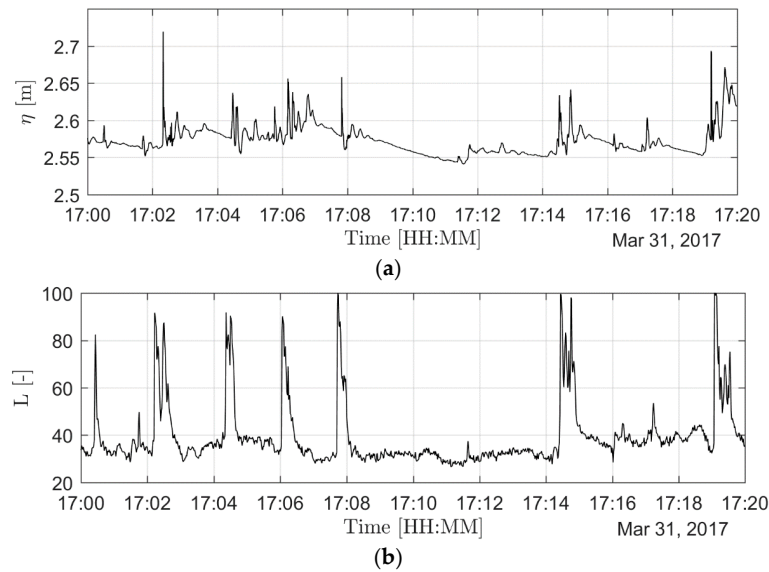


Figure 9. Comparison of (a) water surface elevation time series derived from the pressure transducer data (η), and (b) the pixel lightness metric (L) from the pixel at the transducer deployment location obtained from the rectified camera imagery from 31 March 2017. Water surface elevations are shown relative to the PT location at the bottom of the pool on the rock platform that had a depth of ~ 2.5 m. The PT location shown here was the northeast PT of the two deployed on 29 March 2017 (319,261 m E, 6,214,520 m N). See Figure 2 for location.

4.3. Overwash Analysis

In this paper, we restrict our analysis of wave overwash to the N2 transect, as it is the primary transect of interest that runs directly through the namesake Figure Eight Pool. Wave overwashing hazard analysis for the remaining five transects and the complex interactions between morphology and hydrodynamics at this site are being investigated as part of a complementary study.

Four hydrodynamic parameters were investigated to assess correlations between offshore conditions and platform inundation frequency: (1) significant wave height (H_s), (2) $1.8 H_s$ plus tidal still water level as per equation 5.6 in [25] ($1.8 H_s + \text{SWL}$), (3) the square root of significant wave height multiplied by wavelength derived from the spectral mean wave period ($\sqrt{H_s L_{m01}}$), and (4) $\sqrt{(1.8 H_s + \text{SWL}) L_{m01}}$.

Cross-platform inundation frequency at the Figure Eight Pool (XPIF at $x = 16$ m) was strongly correlated with the local hydrodynamic conditions with XPIF increasing with increases in all four hydrodynamic parameters with significant positive correlations (Figure 10). Nearshore H_s and $1.8 H_s + \text{SWL}$ (Figure 10a,b) had the highest coefficients of determination of 0.55 and 0.57 respectively. Lower, but still statistically significant, correlations were observed for $\sqrt{H_s L_{m01}}$ and $\sqrt{(1.8 H_s + \text{SWL}) L_{m01}}$ (0.48 and 0.51 respectively; Figure 10c,d). In general, XPIF ($x = 16$ m) remained close to XPIF = 0% until $H_s > 1$ m (exceeded 66.5% of the time) or $1.8 H_s + \text{SWL} > 0.5$ m after which XPIF increased rapidly with the Figure Eight Pool approaching very high levels of inundation (XPIF > 60%) for $H_s > 2$ m (exceeded 13.8% of the time) or $1.8 H_s + \text{SWL} > 2.5$ m. For a given wave height, larger peak wave periods (point colors in Figure 10a,b) are more likely to be associated with greater frequencies of inundation but with significant variability.

The influence of wave period (through wavelength) on platform inundation was assessed by the use of $\sqrt{H_s L_{m01}}$, which is commonly used in wave runup investigations on sandy beaches (e.g., [26,27]), as well as a modified version that incorporates SWL, $\sqrt{(1.8 H_s + \text{SWL}) L_{m01}}$. XPIF at $x = 16$ m remained close to XPIF = 0% for low values of $\sqrt{H_s L_{m01}}$ and $\sqrt{(1.8 H_s + \text{SWL}) L_{m01}}$ then increased rapidly with increasing $\sqrt{H_s L_{m01}}$ and $\sqrt{1.8(H_s + \text{SWL}) L_{m01}}$ (Figure 10c,d). The coefficients of determination

for the comparison of XPIF ($x = 16$ m) with $\sqrt{H_s L_{m01}}$ and $\sqrt{(1.8H_s + SWL)L_{m01}}$ were 0.48 and 0.51 respectively, lower than those of H_s and $1.8H_s + SWL$ but still statistically significant. No clear trends were observed with respect to the influence of peak wave direction on inundation frequency (see point colors in Figure 10c,d).

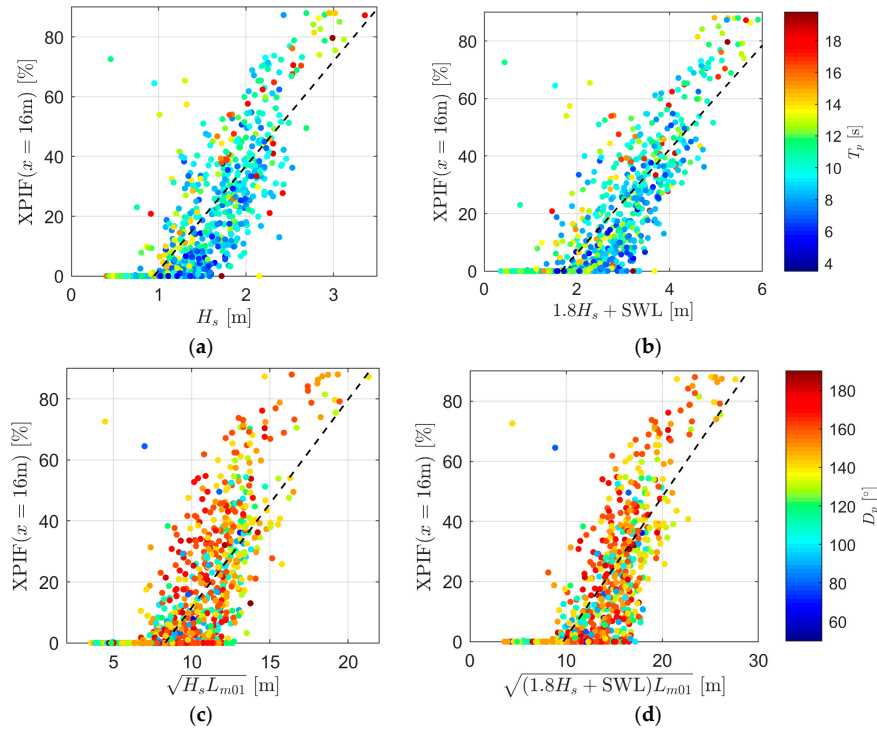


Figure 10. Comparison of inundation on the platform at the Figure Eight Pool location (XPIF at $x = 16$ m on transect N2, see Figure 2 for location) with: (a) significant wave height (H_s); (b) $1.8H_s$ plus tidal still water level ($1.8H_s + SWL$); (c) square root of significant wave height times wavelength derived from the spectral mean wave period ($\sqrt{H_s L_{m01}}$); and (d) $\sqrt{(1.8H_s + SWL)L_{m01}}$. The points in panels (a,b) are colored by peak wave period (see color bar in panel (b)). The points in panels (c,d) are colored by peak wave direction (see color bar in panel (d)). Linear regression lines calculated using data with XPIF $\geq 1\%$ are shown in each panel and correspond to: (a) XPIF = $35.0 H_s - 33.1$, $R^2 = 0.55$; (b) XPIF = $18.1(1.8 H_s + SWL) - 30.0$, $R^2 = 0.57$; (c) XPIF = $6.3\sqrt{H_s L_{m01}} - 45.0$, $R^2 = 0.48$; (d) XPIF = $4.7\sqrt{(1.8 H_s + SWL)L_{m01}} - 45.4$, $R^2 = 0.51$. All linear regression equations have $p < 0.001$.

Cross-platform inundation frequency at $x = 5$ m was also strongly correlated with the local hydrodynamic conditions (Figure 11) with XPIF increasing with increases in all four hydrodynamic parameters with significant positive correlations. Nearshore H_s and $1.8H_s + SWL$ (Figure 11a,b) had the highest coefficients of determination of 0.69 and 0.70 respectively. With a few exceptions, XPIF remained close to XPIF = 0% until $H_s > 0.8$ m (exceeded 83.2% of the time) or $H_s + SWL > 0.6$ m. XPIF increased rapidly relative to both parameters with the platform approaching near complete inundation (XPIF $> 60\%$) for $H_s > 1.8$ m (exceeded 19.7% of the time) or $H_s + SWL > 2.3$ m. For a given wave height, larger peak wave periods (as per the point colors in Figure 11a,b) are more likely to be associated with greater frequencies of inundation, however, there is significant variability.

As with the comparisons of XPIF($x = 16$ m) with $\sqrt{H_s L_{m01}}$ and $\sqrt{(1.8H_s + SWL)L_{m01}}$, XPIF($x = 5$ m) remained close to XPIF = 0% for low values of $\sqrt{H_s L_{m01}}$ and $\sqrt{(1.8H_s + SWL)L_{m01}}$ then increased rapidly with increasing $\sqrt{H_s L_{m01}}$ and $\sqrt{(1.8H_s + SWL)L_{m01}}$ (Figure 11c,d). The coefficients of determination for the comparison of XPIF($x = 5$ m) with $\sqrt{H_s L_{m01}}$ and $\sqrt{(1.8H_s + SWL)L_{m01}}$ were 0.46 and 0.48 respectively, lower than those of H_s and $1.8H_s + SWL$ but still statistically significant.

No clear trends were observed with respect to the influence of peak wave direction on inundation frequency (see point colors in Figure 11c,d).

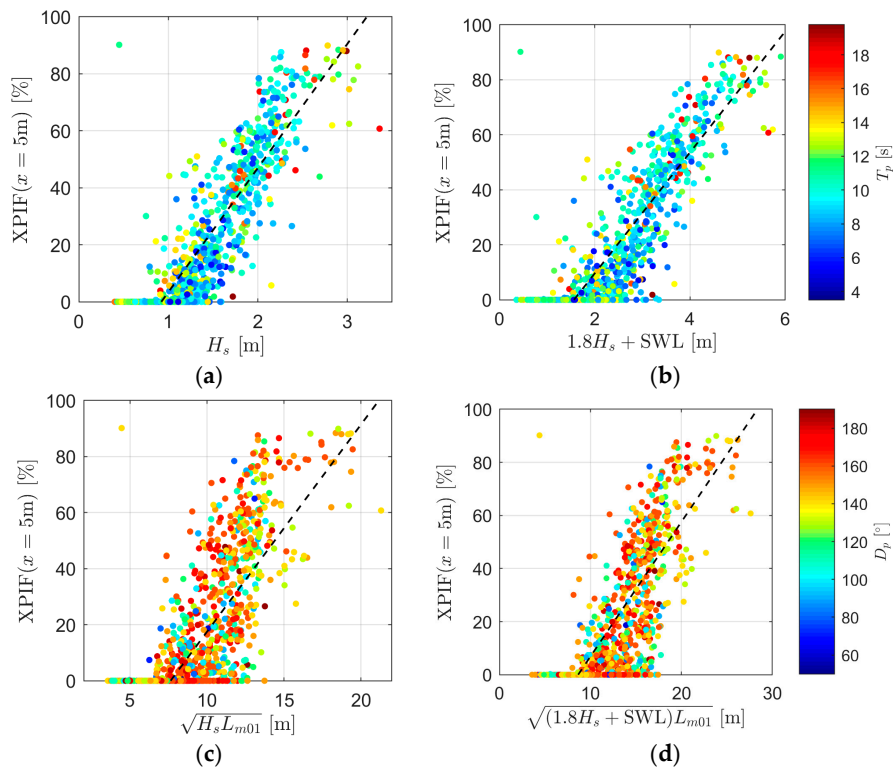


Figure 11. Comparison inundation on the platform at $x = 5$ m on transect N2 (see Figure 2 for location) with: (a) significant wave height (H_s); (b) H_s plus tidal still water level ($1.8 H_s + SWL$); (c) square root of significant wave height times wavelength derived from the spectral mean wave period ($\sqrt{H_s L_{m01}}$); and (d) $\sqrt{(1.8 H_s + SWL) L_{m01}}$. The points in panels (a,b) are colored by peak wave period (see color bar in panel (b)). The points in panels (c,d) are colored by peak wave direction (see color bar in panel (d)). Linear regression lines calculated using data with $XPIF \geq 1\%$ are shown in each panel and correspond to: (a) $XPIF = 43.5 H_s - 40.1$, $R^2 = 0.69$; (b) $XPIF = 22.0(1.8 H_s + SWL) - 34.4$, $R^2 = 0.70$; (c) $XPIF = 6.8 \sqrt{H_s L_{m01}} - 43.7$, $R^2 = 0.46$; (d) $XPIF = 6.2 \sqrt{(1.8 H_s + SWL) L_{m01}} - 36.6$, $R^2 = 0.48$. All linear regression equations have $p < 0.001$.

5. Discussion

5.1. Camera System and Image Analysis

To the authors' knowledge, this is the first time a camera remote sensing system has been used to investigate wave processes on a rock platform. The advantages of using remote sensing to obtain data at such a site are clearly evident: it reduced the impact of data collection on recreational and aesthetic amenity; it allowed for broad spatial data coverage across the entire area of interest; and, it reduced effort and improved safety in data collection when conditions on the platform were highly hazardous, e.g., wave heights of >3 m were recorded on the platform during some storm events, and conditions were often too dangerous to safely access the platform to deploy fixed wave sensors.

The low-cost camera system described here was highly effective with a total data loss of 31.5 days over a 6.7-month period (13.5 months in total over two cameras) which represents a percentage loss of 7.8%. When data loss did occur, camera system failures were most likely due to periods of low power supply that could potentially be rectified by in situ testing and refinement of the power system prior to deployment which was not possible at this location due to the remoteness of the site. Alternatively, a more stable power source, such as standard mains power, would likely address the limited cases of

camera system failure experienced here. The camera resolution of 3 MP was sufficient for the purposes of this project, however, higher resolution cameras (12 MP) from the same manufacturer are now available and could be used in subsequent studies.

The method derived here for obtaining inundation frequencies is a novel means of semi-automatically extracting wave overwash frequencies from remotely sensed data on a rock platform. Due to the high variability of the appearance of the platform caused by variation of sunlight, rock color, algae presence, and standing water bodies in both space and time, a semi-automated approach was implemented. This was done to avoid the incorrect classification of visible features as wave-driven inundation (see Section 3.2). To demonstrate the high variability in platform appearance, Figure 12 shows two example images of lighting conditions that are challenging for automating the extraction of wave inundation frequencies. The images in Figure 6d,f also show examples of challenging lighting conditions for automated analysis where the platform is partially in shadow. While automated techniques have been used on sandy beaches with wide success (e.g., [28,29]), the factors described here make rock platforms significantly more challenging environments compared to sandy beaches, which are not affected by variation in rock color or algae presence and are rarely affected by standing water bodies or significant partial shadow.

There are several approaches that could be taken to obtain a wave overwash hazard metric for our study site. The approach taken here is a cross-platform inundation frequency (XPIF) representing the time the platform is inundated at each cross-platform location along the transects shown in Figure 2. This has the advantage of capturing both the magnitude and frequency of wave overwashing, i.e., larger waves typically travel farther across the platform and generate more foam, thus resulting in longer duration pixel lightness peaks. This is important as wave driven flows are the source of the primary hazard of interest at this site with hazard increasing with increasing wave heights and periods. As noted in Section 4.3, however, the peaks in the image pixel lightness time series are usually of longer duration than the corresponding peaks in the water surface elevation time series (e.g., see Figure 9), which has the potential to result in overestimation of the duration of inundation. An alternative approach would be to count the number of waves overtopping at each cross-platform location and compare that to the offshore wave period to obtain a metric that describes the proportion of waves that overtop the platform. One challenge with taking this approach would be that two waves overtopping the platform in quick succession may not be distinguished in the pixel analysis due to consistently high lightness values caused by the gradual dispersion of whitewater on the platform (e.g., Figure 9 at 17:06). Thus the pixel lightness data may under-estimate the number of individual wave fronts. A further disadvantage to this alternative method is that it would not be able to capture the magnitude of the waves that overtop. While both these methods have shortcomings, the method applied here is deemed to be fit for the purpose of this project, i.e., for the development of an overwash hazard rating system to improve visitor safety at the site.



Figure 12. Still images from the cameras showing instances where the lighting and pixel color was challenging for automated inundation analysis: (a) north camera at 12:00 on 22 March 2017 showing very bright pixels on the landward edge of the rock platform, and (b) south camera at 07:00 on 22 March 2017 showing high levels of sun glint from both the ocean and the standing water on the platform.

5.2. Overwash Wave Inundation Frequencies

The wave overwash hazard along one cross-platform analysis transect (see N2 in Figure 2) has been investigated relative to measured nearshore hydrodynamic conditions and the analysis of overwash wave inundation frequencies suggest that the Figure Eight Pools Rock Platform is a highly hazardous site, with moderate to significant inundation occurring during mean wave conditions and above, and inundation also occurring during below average wave conditions. Despite the elevation of the platform being predominantly above highest astronomical tide, wave overwash onto the platform commences during relatively low-energy conditions, with cross-platform inundation exceeding 0% at $x = 5$ m once nearshore significant wave height exceeds 0.8 m, a wave height that is surpassed 83.2% of the time (Figure 3a). Moderate levels of inundation resulting from intermittent wave overwashing ($0\% < \text{XPIF} < 50\%$) are observed for wave heights in the range 0.8–1.5 m, which includes the mean and modal wave heights (see Section 2.2). Nearshore wave heights >2.0 m result in significant inundation with these conditions exceeded 13.8% of the time. While nearshore wave height is strongly correlated with inundation on the platform, there is still significant variability in inundation frequencies for a given wave height. For example, for $H_s = 1.6$ m, inundation at $x = 5$ m varies from 1% to $>60\%$. The inclusion of tidal still water level and wave period (through wavelength) with significant wave height in comparisons against platform inundation frequencies results in comparable or reduced correlations (Figures 10 and 11). This suggests that the integrated wave parameters and still water level do not fully explain the variability in inundation along this transect of the platform. Similar trends in inundation frequencies were observed for both the example point locations investigated ($x = 5$ m and the Figure Eight Pool at $x = 16$ m). This indicates that there is significant variability in inundation frequency for a given set of nearshore hydrodynamic conditions and further work is required to identify the cause of this variability. One potential contributor to this variability, that was observed in the image data, is that waves that inundated transect N2 did not always arrive from the seaward edge of the transect and travel in a normal direction relative to the edge of the platform. The N2 transect was at times inundated by waves arriving laterally that had overwashed the platform in the area to the south of transect N2 (see transect N3, Figure 2), which is characterized by lower platform morphology. The potential for lateral overwash at transect N2 may vary with different hydrodynamic conditions, and this may contribute some of the variability in inundation frequency observed in Figures 10 and 11. It should be noted, however, that the variability observed here due to wave overtopping driving inundation is comparable to that observed by other studies that have investigated other nearshore, wave-related parameters such as wave driven run-up and overwash (e.g., [26,27]), wave driven setup (e.g., [30,31]), and the nearshore wave breaker criterion (e.g., [32,33]).

5.3. Development of a Wave Overwash Hazard Rating System

The hourly XPIF profiles are particularly useful for classifying the wave overwash hazard in response to the combined wave and tide conditions, because the profiles provide a direct expression of the extent and frequency of wave inundation across the platform. This is another advantage of the remotely sensed data collected by the camera system that would otherwise only be achievable with a dense array of wave sensors. Compared to the low-cost camera system, such an approach would be an expensive and intrusive approach to collecting a similar dataset. It should be noted that the use of inundation frequency alone is a relatively simplified measure of hazard compared to the measures often used in flood studies, such as the product of flow depth and velocity, however, for the purposes of this work, inundation frequencies are deemed sufficient for use as a proxy for wave hazards.

The XPIF profiles from the dataset described here are being applied to develop a wave overwash hazard rating system for the Figure Eight Pools Rock Platform. Figure 13 provides an example of how the XPIF profile space for transect N2 (see Figure 2 for location) can be classified to distinguish between five overwash hazard levels for the vicinity of the Figure Eight Pool. Five example XPIF profiles associated with different wave and tide conditions are shown, which represent five different hazard levels. Category A (dotted line) represents low overwash hazard (although allows for wave splash

at the edge of the platform), where inundation is absent or restricted to less than 2 m landward from the seaward edge of the platform. Category B (dash-dot line) represents minimal overwash hazard, where inundation is restricted to the raised rampart. Category C (thin solid line) represents moderate overwash hazard, where wave inundation may infrequently (<33% of the time) reach the region of the Figure Eight Pool. Category D (dashed line) represents major overwash hazard, where wave inundation infrequently (<33% of the time) extends past the Figure Eight Pool but not across the entire platform. Category E (thick solid line) represents extreme overwash where wave inundation frequently (>33% of the time) reaches the Figure Eight Pool and/or extends across the whole platform. See Table 2 for further detail on the hazard category definitions. Hazard levels can also be distinguished by the shaded areas in Figure 13, which categorize the wave inundation distance-frequency space. A profile line is designated as belonging to a particular hazard category if the XPIF line terminates within the corresponding shaded area in the distance-frequency space. The five hazard levels can be used to describe the relative risk posed by wave overwash to visitors at the rock pools during each daylight hour captured in the camera dataset. While the hazard categories defined here are site specific, a similar approach could be used to define wave hazards at other rock platform sites.

Table 2. Definitions of the five hazard categories defined for the N2 transect on the Figure Eight Pools Rock Platform and the color and line styles used to delineate the categories in Figure 13.






Hazard Category	Hazard Name	Criteria	Hazard Type	Figure 13 Legend
A	Low	XPIF > 0% for $x < 2$ m; & XPIF = 0% for $x \geq 2$ m	Background hazards	
B	Minimal overwash	XPIF > 0% for $x < 10$ m; & XPIF = 0% for $x \geq 10$ m	Some overwash of outer platform, restricted to rampart. Risk to visitors on the outer platform.	 - . - . -
C	Moderate overwash	XPIF > 0% for $x < 10$ m; & $0 < \text{XPIF} < 33\%$ for $x = 10\text{--}18$ m; & XPIF = 0% for $x \geq 18$ m	Overwash reaches Figure Eight Pool. High risk to visitors on the outer platform. Moderate risk to visitors near the Figure Eight Pool, particularly if they are not paying attention to the ocean.	 —————
D	Major overwash	XPIF > 0% for $x < 10$ m; & $0 < \text{XPIF} < 33\%$ for $x = 10\text{--}18$ m; & $0 < \text{XPIF} < 33\%$ for $x = 18\text{--}30$ m; & XPIF = 0% for $x \geq 30$ m	Overwash extending past Figure Eight Pool. Very high risk to visitors on the outer platform and near the Figure Eight Pool who may suffer severe injuries from being washed across the platform.	 - - - -
E	Extreme overwash	XPIF > 0% for $x < 10$ m; & XPIF > 33% for $x = 10\text{--}30$ m; & XPIF > 0% for $x \geq 30$ m	Overwash extending over the entire platform. Extreme risk to visitors anywhere on the platform. Very high risk of severe injuries from being washed across the platform and potentially washed out to sea.	 —————

Figure 14 shows the time series hazard rating for the first month of the camera dataset, along with the wave height and period measured by the wave buoy deployed in 30 m water depth adjacent to the platform (see Figure 1c for location). Comparison between the hazard category and wave time series shows the correlation between high wave height and/or period, and high hazard level, and vice versa. Intermediate hazard conditions (i.e., Hazard Categories B, C, and D in Table 2) tend to occur when significant wave height is below 2 m, such as during the final week of the time series. The full hazard rating time series based on the camera dataset will be analyzed in the context of the measured wave and water level conditions, to develop a predictive hazard warning tool that can determine the overwash hazard level based on forecast wave and tide conditions.

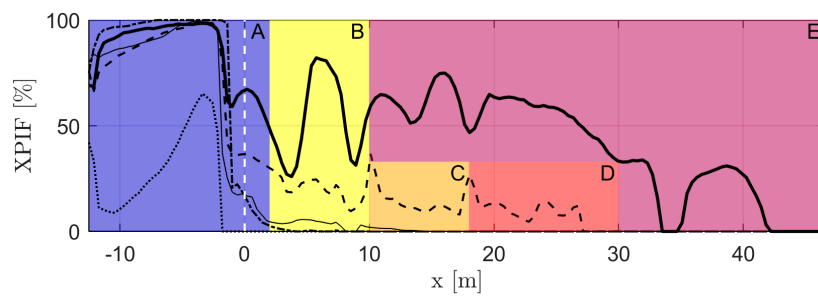


Figure 13. Five examples of XPIFs recorded at transect N2 under different conditions that meet the criteria for the five hazard categories (Table 2): Category A recorded on 22/03/2017 at 12:00 (dotted line), Category B recorded on 26/03/2017 at 16:00 (dash-dot line), Category C recorded on 26/03/2017 at 11:00 (thin solid line), Category D recorded on 23/03/2017 at 12:00 (dashed line), and Category E recorded on 04/04/2017 at 17:00 (thick solid line). The shaded areas represent the five hazard categories defined for transect N2: Category A (blue), Category B (yellow), Category C (orange), Category D (red), and Category E (purple). A profile line terminates (i.e., XPIF goes to 0) in the shaded area of the hazard category to which it belongs, e.g., the dashed line (representing an example XPIF profile for Category D) terminates in the red shaded area at $x \sim 27$ m. The white dashed line represents the edge of the platform at $x = 0$ m. See Section 5.3 and Table 2 for additional detail on the hazard categories.

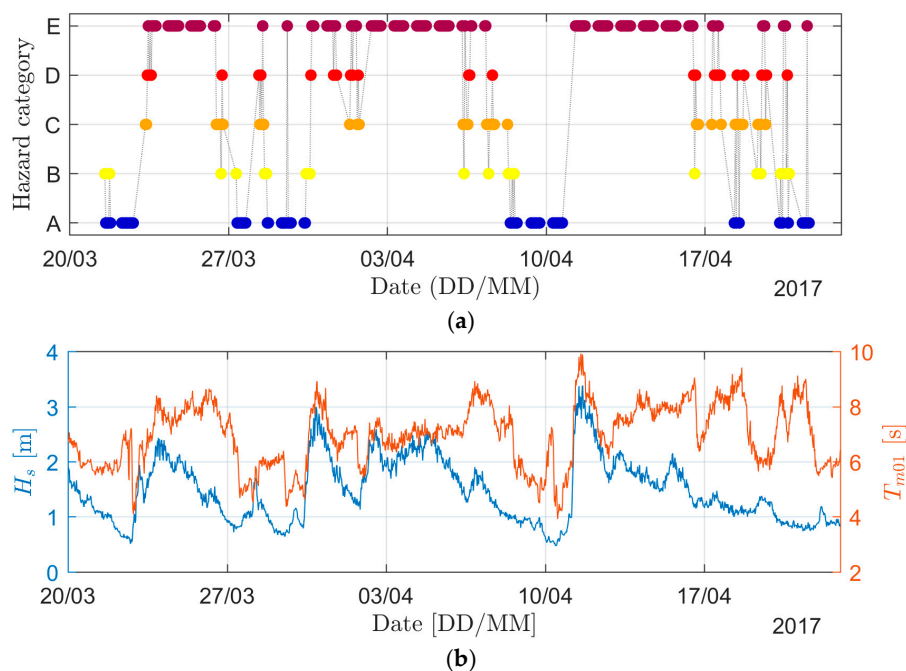


Figure 14. (a) Time series of the hazard category at transect N2 for the first month of camera deployments (21/03/2017 to 21/04/2017). See text in Section 5.3, Figure 13, and Table 2 for further explanation. (b) Time series of significant wave height (H_s ; blue line and left y-axis) and spectral mean wave period based on the first positive moment of the energy spectrum (T_{m01} ; red-orange line and right y-axis) from the wave buoy deployed in 30 m of water offshore of the platform (see Figure 1c for location) for the first month of the camera deployments.

6. Conclusions

A low-cost camera system has been developed and described, and used to capture imagery of wave overwash on an exposed rocky shore platform. The camera system is shown to be both fit for purpose and highly effective with a total data loss of 7.8% over a 6.7-month period and a resolution

sufficiently high for assessing wave inundation on the rock platform. Issues of camera data loss could most likely be resolved with a stable power source (i.e., mains power). Remotely sensed imagery was classified using an automated algorithm that considers pixel lightness and color temperature, with additional manual quality control, to identify the frequency of wave-driven inundation across the platform. Image pixel intensities measured by the camera system correspond well with concurrent, in situ pressure transducer measured water levels across the rock platform.

Nearshore wave height is shown to be the primary factor driving cross-platform inundation frequencies on the Figure Eight Pools Rock Platform (along the cross-platform transect investigated in this paper) with some influence from wave period. Further work is required to assess the more subtle effects of tidal still water level and wave direction on inundation across this rock platform, and the complex interactions between morphology and hydrodynamics at this site are being investigated using the dataset presented here in a complementary study.

A preliminary hazard rating system for the Figure Eight Pools Rock Platform is proposed based on the image data collected by the camera system, and analysis of the first month of data collected suggests that the platform is highly hazardous for visitors. To improve the management of visitor safety, the complete hazard rating time series (derived from the remotely sensed data collected in this study) will be analyzed with concurrent wave and water level data to develop a hazard warning tool that predicts the wave overwash hazard level using forecast wave and tide conditions.

Acknowledgments: This project was funded by the NSW National Parks and Wildlife Service and the Office of Environment and Heritage. The authors thank the management and rangers of The Royal National Park, particularly A. Bianchi, D. Croft, and G. White, for assisting with the design, installation, and maintenance of the camera and power systems. We thank the Sydney Institute of Marine Science and the Water Research Laboratory, UNSW Sydney, for the use of Datawell DWR-G4 wave buoys. Manly Hydraulics Laboratory provided ocean tide and deep-water wave data. We also thank the Academic Research Computing Support Team at the University of Newcastle for support with the I.T. infrastructure on which much of the data analysis was undertaken.

Author Contributions: H.E.P., M.A.K., and D.J.H. conceived and designed the study. H.E.P., M.A.K., C.E.S., and M.J.K. installed the camera systems and hydrodynamic instruments, and collected and analyzed the data. B.D.M. lead the collection and processing of wave data and multibeam bathymetry data. H.E.P. lead the writing of the paper with all authors making contributions.

Conflicts of Interest: This research was funded by the NSW National Parks and Wildlife Service and the Office of Environment and Heritage (OEH). M.A.K., B.D.M., and D.J.H. are research staff of NSW OEH and contributed to the design of the study; the collection, analyses, and interpretation of data; and to the writing of the manuscript.

References

1. Sunamura, T. *Geomorphology of Rocky Coasts*; Wiley: Chichester, UK, 1992.
2. Trenhaile, A.S. *The Geomorphology of Rock Coasts*; Clarendon Press: Oxford, UK, 1987.
3. Beetham, E.P.; Kench, P.S. Field observations of infragravity waves and their behaviour on rock shore platforms. *Earth Surf. Process. Landf.* **2011**, *36*, 1872–1888. [[CrossRef](#)]
4. Shand, T.D.; Peirson, W.L.; Banner, M.L.; Cox, R.J. *Predicting Hazardous Conditions for Rock Fishing a Physical Model Study*; University of New South Wales Water Research Laboratory: Manly Vale, Australia, 2009.
5. Surf Life Saving Australia (SLSA). *Annual Report 2013/14*; Surf Life Saving Australia: Sydney, Australia, 2014.
6. Surf Life Saving Australia (SLSA). *National Coastal Safety Report 2014*; Surf Life Saving Australia: Sydney, Australia, 2014.
7. McArthur, A.G. *Fire Behaviour in Eucalypt Forests*; Department of National Development, Forestry and Timber Bureau: Canberra, Australia, 1967.
8. Holman, R.A. Nearshore remote sensing. In *Proceedings of the Coastal Dynamics*, Tokyo, Japan, 7–11 September 2009; American Society of Civil Engineers: New York, NY, USA, 2009; pp. 37–48.
9. Holman, R.A.; Stanley, J. The history and technical capabilities of argus. *Coast. Eng.* **2007**, *54*, 477–491. [[CrossRef](#)]
10. Poate, T.G.; McCall, R.T.; Masselink, G. A new parameterisation for runup on gravel beaches. *Coast. Eng.* **2016**, *117*, 176–190. [[CrossRef](#)]

11. Shannon, A.M.; Power, H.E.; Webster, J.M.; Vila-Concejo, A. Evolution of coral rubble deposits on a reef platform as detected by remote sensing. *Remote Sens.* **2013**, *5*, 1–18. [[CrossRef](#)]
12. Price, T.D.; Ruessink, B.G. Morphodynamic zone variability on a microtidal barred beach. *Mar. Geol.* **2008**, *251*, 98–109. [[CrossRef](#)]
13. Salmon, S.A.; Black, K.R.; Coco, G. The use of video-systems to measure run-up on beaches. *J. Coast. Res.* **2007**, *50*, 211–215.
14. Power, H.E.; Holman, R.A.; Baldock, T.E. Swash zone boundary conditions derived from optical remote sensing of swash zone flow patterns. *J. Geophys. Res.* **2011**, *116*, C06007. [[CrossRef](#)]
15. Murray, T.; Cartwright, N.; Tomlinson, R. Video-imaging of transient rip currents on the gold coast open beaches. *J. Coast. Res.* **2013**, *65*, 1809–1814. [[CrossRef](#)]
16. Holman, R.A.; Sallenger, A.H.; Lippmann, T.C.; Haines, J.W. The application of video image processing to the study of nearshore processes. *Oceanography* **1993**, *6*, 78–85. [[CrossRef](#)]
17. Kinsela, M.A.; Power, H.E.; Stringari, C.E.; Kendall, M.J.; Morris, B.D.; Hanslow, D.J. Wave Processes and Overwash Hazard on a High-Energy Rock Platform. In Proceedings of the Coastal Dynamics 2017, Helsingor, Denmark, 12–16 June 2017; pp. 685–696.
18. Kennedy, D.M. Where is the seaward edge? A review and definition of shore platform morphology. *Earth Sci. Rev.* **2015**, *147*, 99–108. [[CrossRef](#)]
19. Field, M.E.; Roy, P.S. Offshore transport and sand-body formation: Evidence from a steep, high-energy shoreface, southeastern Australia. *J. Sediment. Petrol.* **1984**, *54*, 1292–1302.
20. Thom, B.G.; Keene, J.B.; Cowell, P.J.; Daley, M. East australian marine abrasion surface. In *Australian Landscapes*; Bishop, P., Pillans, B., Eds.; Geological Society Special Publications: London, UK, 2010; Volume 346, pp. 57–69.
21. Aagaard, T.; Holm, J. Digitization of wave run-up using video records. *J. Coast. Res.* **1989**, *5*, 547–551.
22. Fairchild, M.D. A revision of ciecam97s for practical applications. *Color Res. Appl.* **2001**, *26*, 418–427. [[CrossRef](#)]
23. Sharma, G. (Ed.) *Digital Color Imaging Handbook*; CRC Press: Boca Raton, FL, USA, 2003; p. 816.
24. Kim, Y.; Cho, B.H.; Kang, B.S.; Hong, D.I. Color Temperature Conversion System and Method Using the Same. U.S. Patent 7,024,034, 4 April 2006.
25. EurOtop. *Manual on Wave Overtopping of Sea Defences and Related Structures. An Overtopping Manual Largely based on European Research, but for Worldwide Application*; Van der Meer, J.W., Allsop, N.W.H., Bruce, T., De Rouck, J., Kortenhaus, A., Pullen, T., Schüttrumpf, H., Troch, P., Zanuttigh, B., Eds.; 2016; Available online: www.overtopping-manual.com (accessed on 7 November 2017).
26. Atkinson, A.L.; Power, H.E.; Moura, T.; Hammond, T.; Callaghan, D.P.; Baldock, T.E. Assessment of runup predictions by empirical models on non-truncated beaches on the South-East Australian Coast. *Coast. Eng.* **2017**, *119*, 15–31. [[CrossRef](#)]
27. Blenkinsopp, C.E.; Matias, A.; Howe, D.; Castelle, B.; Marieu, V.; Turner, I.L. Wave runup and overwash on a prototype-scale sand barrier. *Coast. Eng.* **2016**, *113*, 88–103. [[CrossRef](#)]
28. Vousedoukas, M.I.; Wziatek, D.; Almeida, L.P. Coastal vulnerability assessment based on video wave run-up observations at a mesotidal, steep-sloped beach. *Ocean Dyn.* **2012**, *62*, 123–137. [[CrossRef](#)]
29. Vousedoukas, M.I.; Almeida, L.P.M.; Ferreira, O. Beach erosion and recovery during consecutive storms at a steep-sloping, meso-tidal beach. *Earth Surf. Process. Landf.* **2012**, *37*, 583–593. [[CrossRef](#)]
30. Hanslow, D.J.; Nielsen, P. Shoreline set-up on natural beaches. *J. Coast. Res.* **1993**, *15*, 1–10.
31. Nielsen, P. Wave setup: A field study. *J. Geophys. Res.* **1988**, *93*, 15643–15652. [[CrossRef](#)]
32. Robertson, B.; Hall, K.; Zytner, R.; Nistor, I. Breaking waves: Review of characteristic relationships. *Coast. Eng. J.* **2013**, *55*, 466–479. [[CrossRef](#)]
33. Robertson, B.; Gharabaghi, B.; Power, H.E. Predicting breaking wave conditions using gene expression programming. *Coast. Eng. J.* **2017**, *59*, 1750017. [[CrossRef](#)]

